



# Stability and Hazard Assessment of the Progressive Zero Landslide in the Kalimpong Region of Darjeeling Himalaya, India

Suvam Das · Koushik Pandit · Shantanu Sarkar ·  
Debi Prasanna Kanungo

Received: 8 June 2023 / Accepted: 2 September 2023 / Published online: 21 September 2023  
© The Author(s), under exclusive licence to Springer Nature Switzerland AG 2023

**Abstract** Landslides pose serious hazards for mountainous communities. Therefore, slope stability and hazard assessments are imperative for Landslide Disaster Risk Reduction (LDRR). In this study, a progressive landslide, locally known as “Zero landslide” is investigated. This landslide was first initiated on July 16, 2014, and since then its repetitive recurrence has affected a total area of  $1 \times 10^5$  m<sup>2</sup>. Field investigation revealed that different risk elements including a school, residential buildings, and nearby roads are threatened by this landslide. Hence, an attempt has been made for LDRR by incorporating geospatial, engineering geological, and geotechnical approaches. Further, to evaluate the stability of the present slope, finite element modelling (FEM) is used. The multi-temporal satellite image analysis reveals the retrogressive progression of this landslide. Kinematic analysis, Rock Mass Rating (RMR), Geological Strength Index (GSI), and Slope Mass Rating (SMR) methods derived results (RMR = 45, GSI = 25,

SMR = 38.2) indicate that the in-situ geological condition favors the sliding process and has weaker rock mass. In the static loading condition, the FEM based stability analysis predicted lower Factor of Safety (FoS) values i.e., marginally stable in the dry condition (FoS = 1.07) and unstable in the wet condition (FoS = 0.78). The findings of the present study highlight the need to design and implement landslide risk mitigation measures prior to any major event at this particular location.

**Keywords** Landslide · Slope stability · FEM · Hazard and risk · Darjeeling Himalaya

## 1 Introduction

Landslides are defined as the movement of mass under the influence of gravity (Anbalagan et al. 1992; Ansari et al. 2019). The classification of Cruden and Varnes (1996) reveals that landslides can be classified based on failure mode (fall, slide, flow, topple), sliding materials (soil, rock, debris), volume of mass wasted (shallow, deep-seated), and sliding velocity (slow, fast-moving). Landslides can be initialized following a rainfall event (Abraham et al. 2021) and/or triggered by an earthquake (Tesfa 2022; Song et al. 2018), and depending on that their order of magnitude (landslide area/volume) varies (Malamud et al. 2004). In hilly areas, landslides are remarkably hazardous and cause significant damage throughout the

**Supplementary Information** The online version contains supplementary material available at <https://doi.org/10.1007/s10706-023-02641-z>.

S. Das · K. Pandit · S. Sarkar (✉) · D. P. Kanungo  
Academy of Scientific and Innovative Research (AcSIR),  
Ghaziabad 201002, India  
e-mail: shantanu\_cbri@yahoo.co.in

S. Das · K. Pandit · S. Sarkar · D. P. Kanungo  
CSIR-Central Building Research Institute,  
Roorkee 247667, India

world (Kumar et al. 2019; Sardana et al. 2022; Panda et al. 2022). Apart from this, landslides perhaps invite multi-hazard interactions such as dam formation (Kumar et al. 2019), flash floods (Martha et al. 2021), and debris flows (Dash et al. 2021; Abraham et al. 2021); causing socio-economic losses. Compared to other natural hazards (e.g., floods, earthquakes, and forest fires), the occurrence of landslides is mostly limited to hilly areas, however, usually the damages induced by landslides are relatively high. The Oxford Martin School database (<https://ourworldindata.org/natural-disasters>, assessed on Dec 09, 2022) shows landslides have caused a global economic loss of over US \$11 billion in the past 41 years (1980–2021). However, not every landslide is hazardous and the hazard level generally depends on its location and interaction with risk elements (Kanungo et al. 2013; Martha et al. 2021). Similarly, landslides are highly dynamic over space and time (Malamud et al. 2004); a small landslide may turn into a larger failure or a landslide may reach a stable state after the initial failure. Thus, it is imperative to assess the existing landslides and determine their stability for future risk evaluation.

The tectonically unstable Himalayan Mountain region favors frequent landslides in all forms and shares 30% of global economic losses (Singh et al. 2018). Intense rainfall events and occasional earthquakes increase the vulnerability to landslides in the Himalayan region as well as other landslide prone areas of India (Anbalagan et al. 1992; Kanungo et al. 2013; Pain et al. 2014; Martha et al. 2021; Mandal and Sarkar 2021). Population growth and allied infrastructure developmental activities have increased the landslide hazard exposure level and every year huge damages are getting reported (Kanungo et al. 2008). According to the Indian Ministry of Home Affairs Disaster Management Division database (<https://ndmindia.mha.gov.in/NDMINDIA-CMS/viewW/hatsNewPdf-D935>, assessed on Dec 09, 2022), 182 fatalities due to landslides are reported in the year 2022. Therefore, it is of great importance to investigate landslides for risk mitigation. Landslides and their mechanisms are very complex, and governed by the interaction of the surface and sub-surface processes. The available methods used in landslide investigation range from spatial scale to site-specific domain. Spatial scale investigations often use remote sensing data products to identify the landslide

probable areas. Such analysis inherently involves empirical as well as statistical methods, and based on that, different certainty level-based predictions are made (Das et al. 2022). Despite their prevalence in predicting landslides, the available methodologies are often restricted in explaining the site-specific conditions (Kanungo et al. 2013). Moreover, such spatial investigations are only suitable for dealing with the population of landslides and their regional patterns. Therefore, it is evident that site-specific studies and in-situ investigations are more desirable (Anbalagan et al. 1992; Tandon et al. 2022). To date, different methods are available for landslide in-situ investigation, and they can broadly be categorized into two groups, namely the empirical and numerical methods. A wide array of empirical methods has been proposed for kinematic analysis, rock mass characterization, and slope stability assessments. The commonly practiced approaches are Rock Mass Rating (RMR), Slope Mass Rating (SMR), and Geological Strength Index (GSI) based methods (Romana 1985; Bieniawski 1989; Anbalagan et al. 1992; Sonmez and Ulusay 2002). The parameters used in these approaches are rating/weightage based and are often decided by expert judgments. Therefore, the parametric ratings may vary depending on individual interpretation and often serve as a preliminary explanation of the studied landslide(s). Following this, with advancement in computational power, different numerical approaches like Limit Equilibrium Method (LEM), and Finite Element (FE) based methods are also used (Singh et al. 2018; Hu et al. 2019; Tandon et al. 2022). Numerical methods aim to compensate for the ad-hoc subjectivity involved in the empirical methods and offer more reliable predictions (Kanungo et al. 2013; Pain et al. 2014). However, such methods are data-intensive and require different lab-based results for robust prediction.

In the present study, the Zero landslide located in the Nimbong village of Kalimpong region of Darjeeling Himalaya has been investigated (Fig. 1). After the first initiation on July 16, 2014, this landslide affected a total area of  $1 \times 10^5 \text{ m}^2$  so far, and have destroyed stretches of local roads and four households. The repetitive reactivation of this landslide poses a constant threat to the local communities. To date, no site-specific investigation is carried out in this area. Therefore, the present study strives to explain the evolution process, in-situ rock and soil properties,

**Fig. 1** Aerial view (Google Earth image) of the Zero landslide with associated risk elements



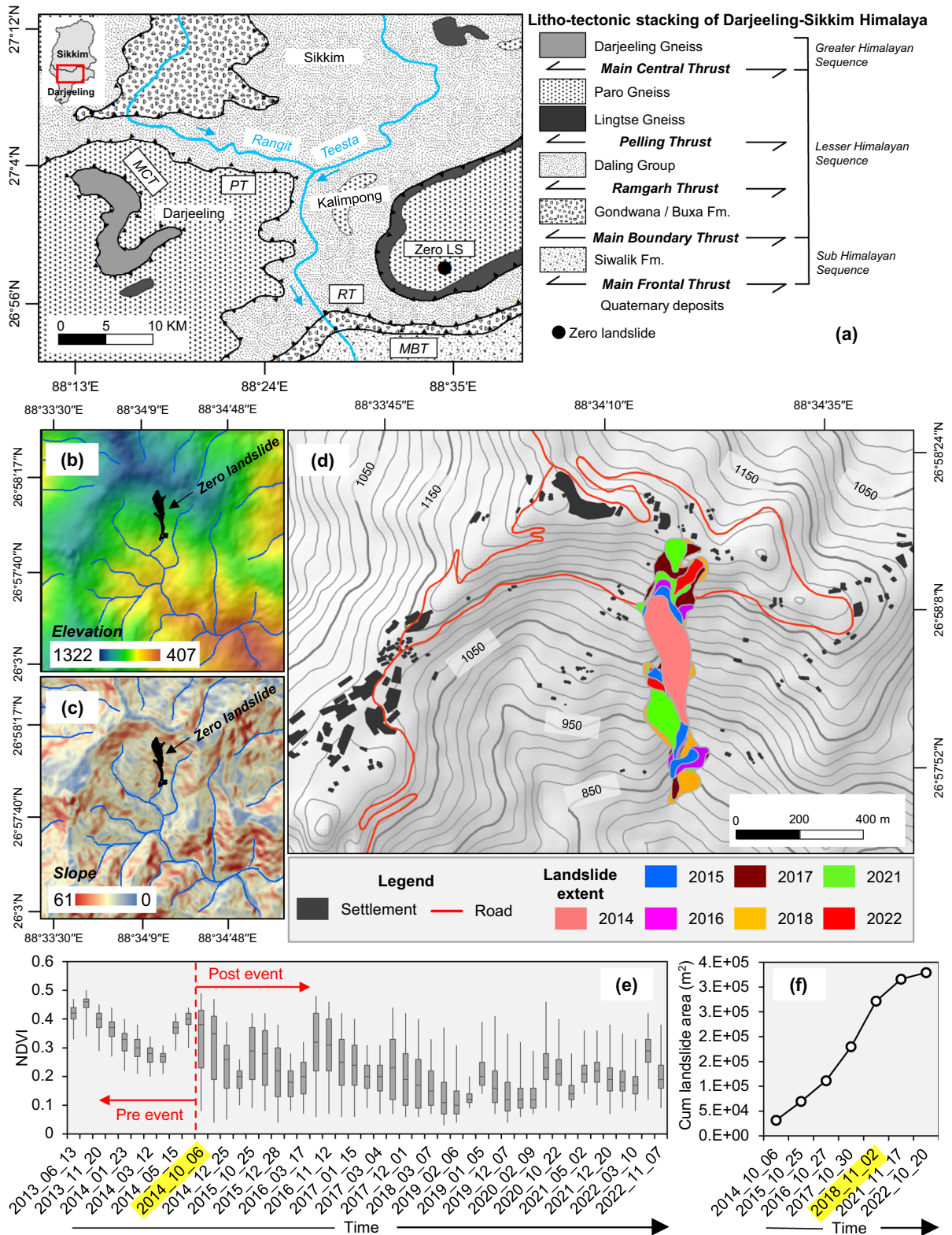
probable causes, stability status and expected future risk conditions of this landslide. For this, a historical database was prepared based on satellite images, followed by empirical and numerical methods for stability assessment. Here, Finite Element Modelling (FEM) based analysis was used to provide more competent insights into the present stability status of the slope. Following this, pore pressure coefficient ( $R_u$ ) based FEM analysis has also been carried out to evaluate the slope stability during rainfall conditions. Finally, the results are discussed in this present context and the associated risks are highlighted. The outputs from this study are expected to be relevant for the end-users and local authorities to implement landslide risk mitigation measures prior to any major event at this particular location.

## 2 Study Area

Rugged terrain, steep slopes, weak geological condition, frequent earthquakes, and heavy seasonal precipitation often resulted in extensive landslides and progressive surface displacements in the Kalimpong region (Mandal and Sarkar 2021; Das et al. 2022). Short temporal frequency and high magnitude of landslides have greatly affected the developmental activities of this region. The present study area is known as

Nimbond village located about 15 km southeast of the Kalimpong town, on the right bank of the Teesta River (Fig. 2a). This area has a sub-tropical climate and is strongly influenced by the Indian Summer Monsoon (ISM). The annual rainfall varies with average rainfall intensity of around 10 mm/day, and due to the ISM circulation, maximum rainfall (about 80%) is showered between June to September period. Using the Rainfall Seasonality Index (RSI) proposed by Walsh and Lawler (1981), a value of  $0.68 \pm 0.03$  was obtained for this area. And according to Walsh and Lawler (1981), the result indicates that rainfall is seasonal in this area. Although, the historical database shows that a maximum daily rainfall of 521 mm in the year 1950 and 304 mm in the year 1968 were recorded in this area. Details on rainfall information are provided in the supplementary materials (S1.). Such intense rainfalls often caused local landslides and previous studies (e.g., Mandal and Sarkar 2021) showed that a minimum rainfall of 21 mm/day (0.88 mm/h) is sufficient to trigger a landslide in this area. Geologically, the area is a part of the Lesser Himalayan Sequence, and the underneath lithology is mainly composed of moderate to highly weathered Paro Gneiss rock. The rocks belonging to this group have Palaeo Proterozoic age followed by the intrusive Lingtse Gneiss. Stratigraphically, these rock groups are thrust over the schist and slate dominated by Daling Group, and the Main Central Thrust (MCT)





◀**Fig. 2** Study area: **a** Litho-tectonic setup of Darjeeling-Sikkim Himalaya; **b** elevation and **c** slope map of the study area; **d** multi-temporal inventory of the Zero landslide; **e** NDVI based assessment of the landslide; and **f** cumulative landslide affected area in different temporal periods

is marked as a separation boundary between them. The regional geological map modified after Bhattacharyya et al. (2015) is shown in Fig. 2a. The litho-tectonic map (Fig. 2a) shows an abundant concentration of thrust zones in this area and the rock structures are ranging from Pre-Cambrian (Darjeeling Gneiss) to Quaternary sediments. As per the IS code 1893 (Part 1): 2016, this area has been referred to as seismically active and attributed to the Zone IV category. In the recent past, an earthquake of  $M_w$  6.9 occurred in the neighboring Sikkim area, which supports the active tectonics of this region. The soil texture of this area is governed by the sub-surface lithology and primarily belongs to the gravelly loamy to loamy skeletal group (Source: National Bureau of Soil Survey and Land use Planning, Kolkata). During the field survey, it is observed that the soil depth is not uniform throughout the area and varies from  $<1$  m to  $>5$  m, depending on the slope angle. The topographic layout of the area shows high relief contrast (Fig. 2b), having maximum elevation in the Northern parts ( $\sim 1322$  m) and gradually decreasing towards the south ( $\sim 407$  m). The elevation of the area decreases rapidly over a shorter distance and indicates the presence of steep slopes. The slope map (Fig. 2c) of the area shows a maximum slope gradient of  $\sim 61^\circ$  (Fig. 2a) and formed deep-narrow valleys followed by extended ridges. In this area, drainage concentration is very high (Fig. 2b and c), and mostly belong to first and second-order channels. During the field survey, the identified channels are revealed as intermittent as well as perennial in nature. Steep slopes and high drainage density favor intense fluvial erosion and often resulted in landslides (Kanungo et al. 2008). The area has isolated settlement units, mostly located along the ridge tops and connected with surrounding areas with metallic and un-metallic roads.

### 3 Landslide Characteristics and Geological Setting

The Zero landslide is located at  $26^\circ 58' 11.30''$ N and  $88^\circ 34' 16.90''$ E (Fig. 2d) and was first activated on

July 16, 2014. Normalize Difference Vegetation Index (NDVI) based temporal investigation reveals that the landslide was coherently deformed (Fig. 2e and f) and progressed retrogressively towards the uphill section by modifying its shape and dimension (Fig. 2d). The landslide initiated at the upstream section of a first-order channel and extended downhill in the direction of  $N176^\circ$  by damaging the existing roads, human settlements, and agricultural lands (Fig. 1). The initiation and successive reactivations of this landslide were accompanied by heavy rainfall events during the ISM periods. Although, the exact dates of the reactivations were not obtainable from the historical dataset. Field photographs of the present landslide slope are shown in Fig. 3. In the crown section, multiple longitudinal tension cracks having lengths of 80–164 cm and widths of 7–13 cm were observed (Fig. 3). The development of such cracks supports the fact that this landslide is still active and continuously progressing. Above the crown section, a school and many human settlements are situated and below it, a connecting road between Kalimpong town and Bagrakot is located (Fig. 1). At present, the crown and toe section of this landslide is at an elevation of  $\sim 1254$  m and  $\sim 812$  m, respectively with a lateral distance of  $\sim 820$  m. Considering the geo-material involved in the sliding process, this landslide can be attributed to a rock-cum-debris slide. Following the types of movement as suggested by Cruden and Vernes (1996), different movement patterns are observed in the main sliding area. At the crown section, the movement appears to be as rotational and in the lower section, multiple translational slides in both flanks entrained the debris in the main landslide body (Fig. 1). To date, this landslide has affected a total area of  $1 \times 10^5$  m<sup>2</sup> and achieved a maximum width of  $\sim 178$  m (Fig. 2d). Based on the field survey, the average depth of the sliding mass was determined, which comes out to be approximately 9 m and becomes maximum in the upper section ( $\sim 15$  m). The bedrock lithology is composed of gneissic rock, characterized by moderate to high weathering rate (Fig. 3). The exposed rock structure in both flanks shows an abundant concentration of disintegrated joint planes having low persistence (Fig. 3). In the recent past (the 2011 Sikkim earthquake,  $M_w$  6.9), this landslide zone (Nimbong area) was subjected to strong seismic motion. Using the attenuation relationship of Fukushima and Tanaka (1990), for this earthquake event the estimated peak



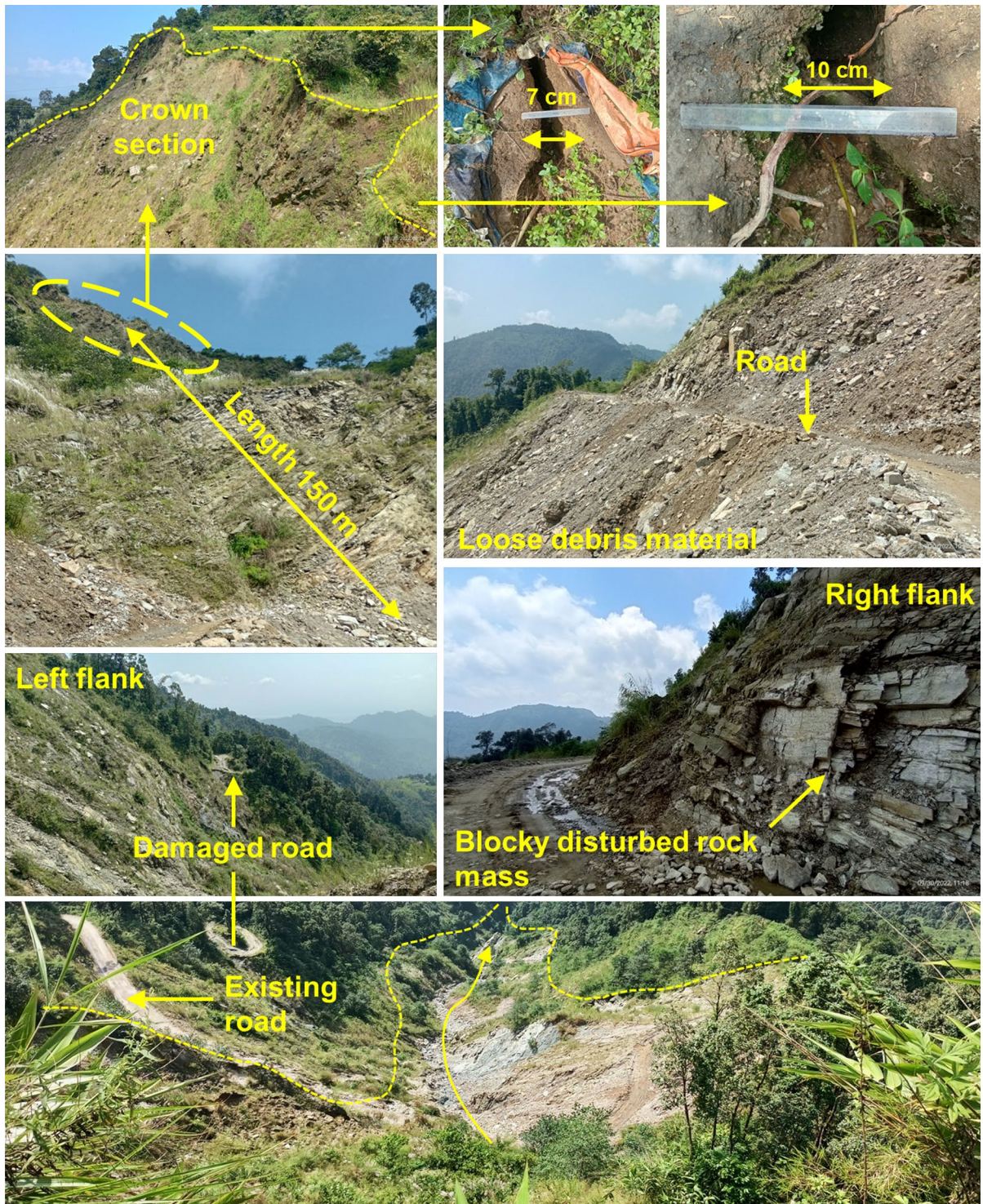


**Fig. 3** Field photographs of the Zero landslide area



horizontal acceleration was found to be  $\sim 1.81 \text{ cm/s}^2$  for this area (the reader is referred to the supplementary materials for details, S2.). Such an intense ground motion may be responsible for weakening the ground rigidity, and owing to the close proximity of thrust and faults, the rock structures are expected to be deformed. To estimate the volume of this landslide, the ellipsoidal semi-axis method (Eq. 1) proposed by Cruden and Varnes (1996) was used. The estimated volume is approximately  $1.04 \times 10^5 \text{ m}^3$ , mainly released from the crown section.

$$V_L = \frac{1}{6} \pi D_d \cdot W_d \cdot L_d \tag{1}$$

where  $V_L$  is the volume of the landslide;  $L_d$  is the minimum distance between the crown and toe;  $W_d$  is the maximum breadth of the displaced mass perpendicular to the length  $L_d$ ; and  $D_d$  is the maximum depth of the displaced mass measured perpendicular to the plane containing  $W_d$  and  $L_d$ . The sliding velocity of the landslide was estimated using the Eq. 2 (Scheidegger 1973) without considering the effect of pore water pressure in shear resistance:

$$v = \sqrt{2g(H - f \times L)} \tag{2}$$

where  $v$  is the estimated sliding velocity (m/s);  $g$  is the gravitational acceleration;  $H$  is the vertical height difference between the starting point and the estimating point;  $f$  is the tangent of effective friction angle or angle of reach, which is the angle of the energy line starting from the highest point (top of the landslide) to the most distant point (toe of the landslide); and  $L$  is the horizontal distance between the starting point and the estimating point. The obtained velocity profile (Fig. 4) shows a gradual increase up to a horizontal distance of 550 m with a vertical drop height of 319 m and achieved a maximum velocity of 21.05 m/s, and after this point velocity decreases rapidly towards the toe section.

Based on the field observation and existing morphological appearance of the landslide, different material boundaries are determined. At the top section, relatively thick ( $\sim 15 \text{ m}$ ) post-sliding materials mainly composed of soil and debris were observed. The upper layer is upheld by a successive debris cover ( $\sim 10 \text{ m}$ ), which is positioned towards the downhill road. Near the road section, in-situ rocks are exposed followed by highly jointed gneiss and extended in the

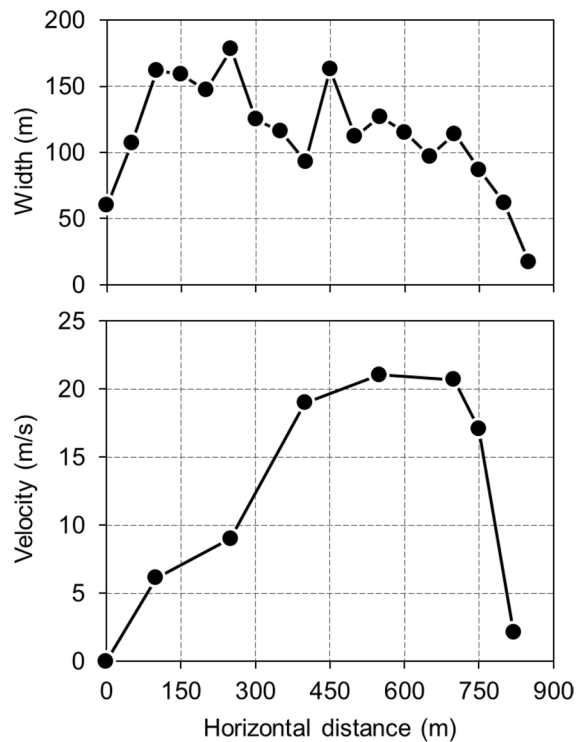


**Fig. 4** Landslide width and estimated landslide velocity (m/s) along the movement direction

lower valley section. Based on the oral testimonies of local residents, it is known that the previous activations of this particular landslide did not claim any life; however, it caused huge socio-economic damage. Additionally, the remote location of Nimbong village makes it more vulnerable to landslide risk than the surrounding areas.

### 4 Materials and Methods

To provide reliable insights into the stability assessment of the studied landslide, an intensive field investigation with geospatial, engineering geological, and geotechnical investigations have been carried out. A detailed description of them is presented in the following sections.

#### 4.1 Geospatial Analysis

To interpret the temporal changes a total of 47 Landsat-8 OLI satellite images were obtained (downloaded

from <https://glervis.usgs.gov/app>, assessed on Nov 25, 2022), from 2013 to 2021 (details are provided in the supplementary materials, S3). All these images are used to delineate the temporal progression of the landslide. Along with this different ancillary earth observation information like ALOS PALSAR DEM (downloaded from <https://search.asf.alaska.edu/#/>, assessed on Dec 24, 2022) and Google Earth Pro (@Google.Inc) based products are also used.

## 4.2 Engineering Geological Investigation

In this study, kinematic analysis, Rock Mass Rating ( $RMR_{basic}$ ) and Geological Strength Index (GSI) methods were used to evaluate the rock mass, whereas, the Slope Mass Rating (SMR) method is used to estimate the failure potential.

### 4.2.1 Kinematic Analysis

For kinematic analysis, the slope and joint orientation (dip/dip direction) were measured using the Brunton compass and then plotted in a stereographic projection using the Dips software (<https://www.rocscience.com/software/dips>) to find the critical failure envelope. Here, Markland's test referred to by Hoek and Bray (1981) was used for kinematic analysis.

### 4.2.2 Rock Mass Rating ( $RMR_{basic}$ )

To estimate the  $RMR_{basic}$  proposed by Bieniawski (1989), the following five parameters are required: (i) uniaxial compressive strength (UCS); (ii) rock quality designation (RQD); (iii) spacing of discontinuities; (iv) condition of discontinuities; and (v) groundwater condition. To determine the UCS, point load testing was carried out on the rock lumps collected from the field. As suggested by Tandon et al. (2022), size corrected point load strength ( $I_{S50}$ ), equivalent to a diameter of 50 mm has been determined (Fig. 5) for each sample ( $UCS = 24 \times I_{S50}$ ). Next, the number of joints per cubic meter area ( $J_v$ ) was counted, and using the empirical relation given by Palmstrom (2005) the RQD was estimated ( $RQD = 110 - 2.5J_v$ ). The discontinuity properties and groundwater conditions were directly measured from the field.

### 4.2.3 Geological Strength Index (GSI)

For estimating the GSI of the rock mass, a quantitative GSI chart given by Sonmez and Ulusay (2002) was used. For doing this, structural rating (SR) and surface condition rating (SCR) were derived using the following relations given in the chart.

$$SR = -17.5 \ln(J_v) + 79.8 \quad (3)$$

$$SCR = R_r + R_w + R_f \quad (4)$$

The roughness condition ( $R_r$ ), weathering condition ( $R_w$ ), and infilling ( $R_f$ ) information were directly collected from the field. Thereafter, the pair of SR and SCR needs to specify in the Cartesian plane of the GSI chart and their intersecting point indicates the corresponding quantitative GSI value.

### 4.2.4 Slope Mass Rating (SMR)

Further to assess the failure potentiality, the SMR technique developed by Romana (1985) and modified by Anbalagan et al. (1992) was utilized. The SMR can be obtained using the following equation:

$$SMR = RMR_{basic} + (F_1 \cdot F_2 \cdot F_3) + F_4 \quad (5)$$

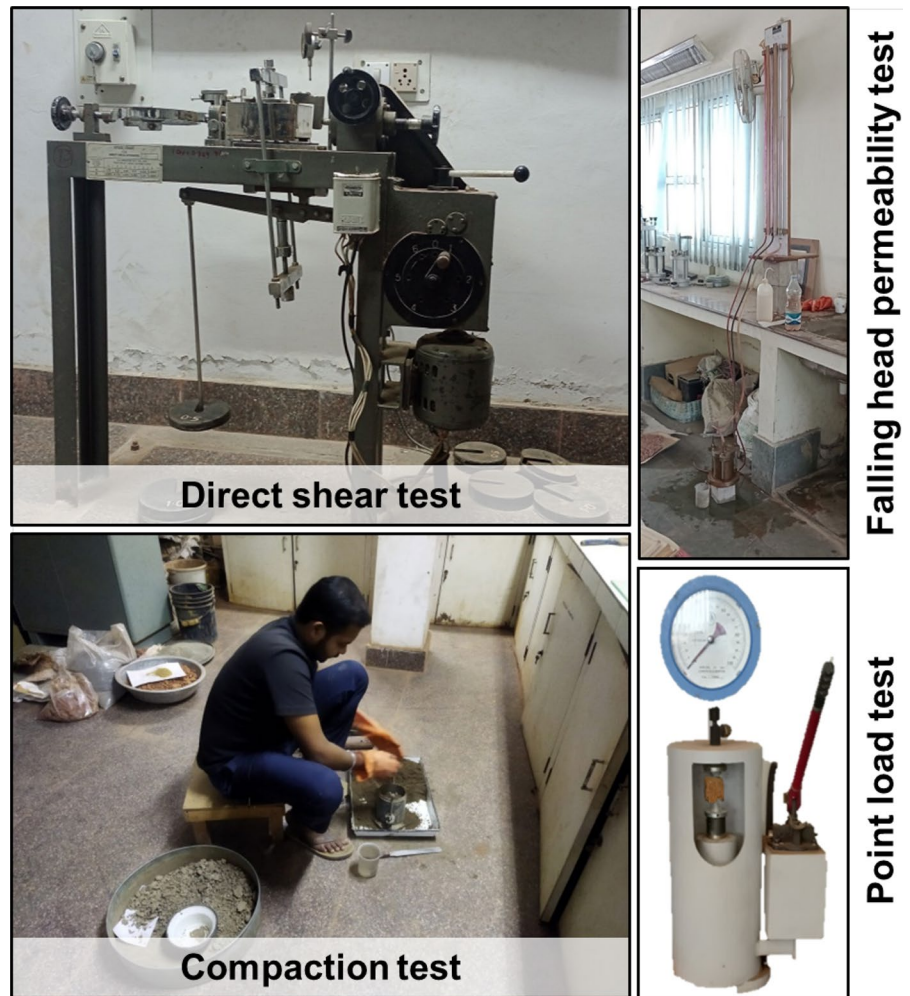
where  $F_1$  refers to the parallelism between the joint dip direction ( $\alpha_j$ ) or plunge line ( $\alpha_i$ ) with the dip direction of the slope face ( $\alpha_s$ );  $F_2$  refers to the dip of the joint ( $\beta_j$ ) or plunge line ( $\beta_i$ );  $F_3$  refers the relationship between the joint dip ( $\beta_j$ ) or the plunge line dip ( $\beta_i$ ) with the slope dip ( $\beta_s$ ); and  $F_4$  refers the adjustment factor (excavation method), ranging from +15 (natural slope) to -8 (deficient blasting).

## 4.3 Geotechnical Investigation

Soil samples collected from the crown section (S1) and above the road section (S2) were tested in the laboratory to determine the important geotechnical properties. All tests were performed according to the Indian Standards (IS 2720, Bureau of Indian Standards). A detailed description of the tests is provided in the following sections.



**Fig. 5** Lab tests of the collected soil and rock samples



#### 4.3.1 Grain Size Analysis

For this study, sieve sizes of 4.75 mm, 2.36 mm, 1.18 mm, 0.60 mm; 0.425 mm, 0.30 mm, 0.15 mm, and 0.75  $\mu\text{m}$  were used to determine the particle size distribution. Depending on their characteristics (i.e., gravel, sand, clay, and silt), the soils can be classified into different groups.

#### 4.3.2 Atterberg Limits

Atterberg limits are intended to measure the behavior of soil (solid, semi-solid, plastic, and liquid state) at different moisture levels. For this study, Casagrande's apparatus was used to find the liquid limit (LL) of the collected soil samples. LL defines the moisture content at which soil behaves like a liquid.

#### 4.3.3 Proctor Compaction Test

The purpose of the compaction test is to determine the Maximum Dry Density (MDD) of soil at certain moisture content. This moisture level is called Optimum Moisture Content (OMC). At the MDD state, all void spaces present in the soil are replaced by the water, and soil particles become closely packed. Above the OMC level, the MDD starts decreasing as excess water start displacing the soil particles. In this study, the soil samples are initially tested at 8% of water content, and then, it was gradually increased at a 2% interval to find the OMC and MDD values (Fig. 5).

#### 4.3.4 Direct Shear Test

To determine the shear strength parameters i.e., cohesion ( $c$ ) and angle of internal friction ( $\phi$ ) of the collected soil samples the direct shear test was carried out. Considering the OMC and MDD values the samples are prepared and sheared at a rate of 0.625 mm/min under the undrained condition. During the test, four vertical loadings equivalent to the normal stresses of 0.5, 1, 1.5, and 2 kg/cm<sup>2</sup> were applied (Fig. 5) and the obtained failure envelopes were plotted according to the Mohr-Coulomb theory ( $\tau = c + \sigma \tan \phi$ ; where  $\tau$  is the shear strength,  $c$  is the cohesion,  $\phi$  is the friction angle, and  $\sigma$  is the applied normal stress) to determine the  $c$  and  $\phi$ .

#### 4.3.5 Permeability Test

A permeability test is performed to gain the soil hydrological characteristics. The permeability depends on the particle size and shape or void spaces present in the soil. For this study, permeability tests were conducted using the falling head method (Fig. 5).

### 4.4 Finite Element Analysis

The stability of a slope inherently depends on the combined effect of driving forces (triggering factors like rainfall and earthquake) and resisting forces (shear strength properties). The Factor of Safety (FoS) ratio, i.e.,  $\text{FoS} = \Sigma \text{resisting forces} / \Sigma \text{driving forces}$ ; is analyzed to understand the stability of the slope. Generally,  $\text{FoS} \leq 1$  denotes an unstable slope,  $\text{FoS} \geq 1$  and higher values for a stable slope, and  $\text{FoS} = 1$  represents a marginally stable slope. A schematic diagram of FoS principles is shown in Fig. 6. To determine the FoS of a slope, finite element method (FEM) based numerical modelling is often used by practitioners (Pain et al. 2014; Sarkar et al. 2021). The FEM has many advantages over the limit equilibrium method (LEM), for instance, no assumptions need to be made about the location or shape of the failure surface, slice side forces, and their directions (Kanungo et al. 2013). Similarly, this method allows for the consideration of different material models (Mohr-Coulomb) to simulate complex conditions and give information on progressive failure until the global equilibrium is achieved (Singh et al. 2018; Sarkar et al. 2021). For

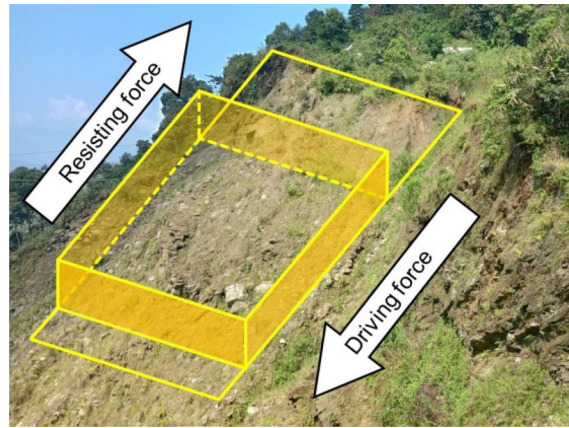
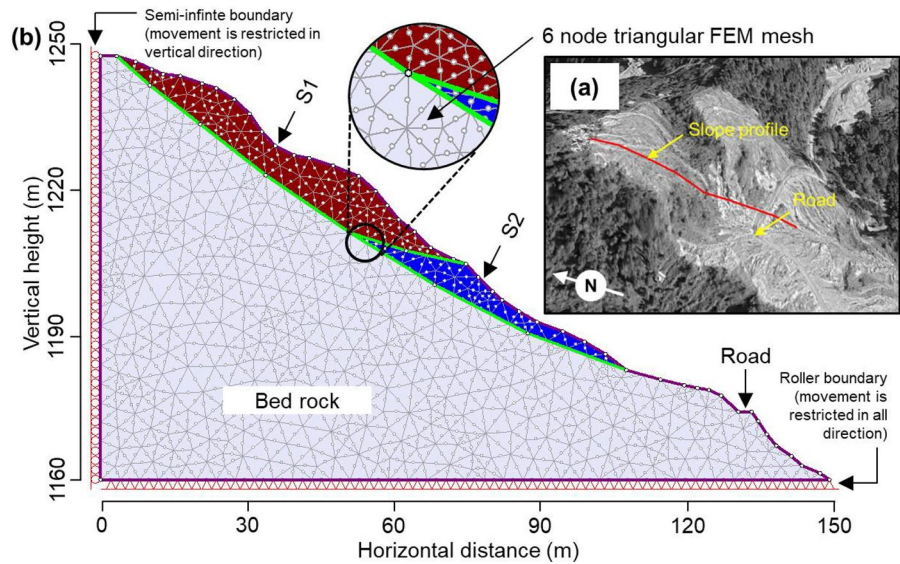


**Fig. 6** Slope stability mechanism in terms of driving force and resisting force

slope stability, the FEM approach has two categories (Hu et al. 2019): (i) the gravity increase method (GIM), and (ii) the shear strength reduction method (SSR). The GIM is used to define the critical failure state (FoS) of the potential slip surface by gradually increasing the gravitational acceleration (Hu et al. 2019). In the SSR method, FoS is defined by reducing the shear strength parameters ( $c$  and  $\phi$ ), until the slope reaches the state of equilibrium (Matsui and San 1992).

In the present study, a slope section of 150 m length starting from the crown section of the landslide to the bottom of the existing road is considered (Fig. 7a) for two-dimensional (2D) FEM analysis. This slope stretch is decided based on field observation, as it shows the potentiality of reactivation. Here, the RS2 software (<https://www.roscience.com/software/rs2>, version 11.017) is used for FE analysis. From the library of the FEM program, 6 noded triangular elements were used to mesh the slope geometry. After discretization, a total of 962 elements and 2031 nodes were assigned (with zero bad elements) for the slope section (Fig. 7b). To simulate the boundary conditions, roller support boundaries were applied on the hill side which can be assumed as a semi-infinite boundary. The valley side or open face is assigned no boundary restrictions. Thus, the side boundary is fixed to move in the horizontal direction, but not in the vertical direction, and the slope face has no movement restrictions. A fixed boundary condition is assigned at the slope bottom so that it cannot move

**Fig. 7** **a** Slope profile used for FEM modelling; **b** FEM configuration used in stability assessment



in any direction. In the next step, the boundaries of slope materials were imported in the profile section and material properties were assigned to them. For soil sections, the Mohr-Coulomb strength criterion was considered and for the rock section, the Generalized Hoek–Brown (GHB) strength criterion was used to define the slope material properties. Using the RS2 library, the Hoek–Brown parameters ( $m_b$ ,  $s$ , and  $a$ ) were directly estimated from the GSI value. The above discussed methodology presents the FEM based slope stability under the dry-static condition. To simulate the saturated condition, the pore water pressure coefficient ( $R_u$ ) is used. This  $R_u$  coefficient is similar to the Skempton pore-water pressure coefficient ( $\bar{B}$ ), and a higher value indicates more saturation and thereby generates more pore water pressure alike rainfall conditions (Bishop and Morgenstern 1960).

**5 Results and Discussion**

The analysis of multi-temporal satellite images clearly indicates the progressive growth of the Zero landslide (Fig. 2d and e). After the first initiation, the total affected area increased by ~46%, and the major progression was observed after the 2018 ISM period (affected an area of  $\sim 9.17 \times 10^4 \text{ m}^2$ ) (Fig. 2f). Notably, the crown section showed the most active progression and become relatively steeper. In the lower part, multiple secondary slides were entrained in the

main landslide and deposited debris in the downhill section. At present, the upper right section shows displacement signatures and increases the risk for the locals.

The field measured orientation of the joints and slope is presented in Table 1 and their stereo plot is shown in Fig. 8. Based on their alignment, planar and wedge failure probabilities were found as 33.33% and 66.67%, respectively. The stereo plot shows J1 and J2 formed a plunge line having a dip/dip direction of  $27^\circ/194^\circ$ , respectively. Following Markland’s criteria, the present slope-plunge line orientation satisfied the critical wedge failure condition (Fig. 8).

To obtain  $RMR_{basic}$ , the five input parameters were defined first. The rock lumps collected from the field were tested in the point load testing machine and then the size corrected UCS values were determined (Table 2). The obtained UCS values range from 88 to 109 MPa with an average of 99.97 MPa. The  $J_v$  was found as 15 and based on this, the corresponding

**Table 1** Joint sets and slope orientation

	Dip/dip direction
Joint sets	
J1	$48^\circ/N260^\circ$
J2	$40^\circ/N147^\circ$
J3	$74^\circ/N210^\circ$
Slope	$50^\circ/N176^\circ$



**Fig. 8** Stereonet plot of the slope and joints (J1, J2, and J3) orientation (dip/dip direction)

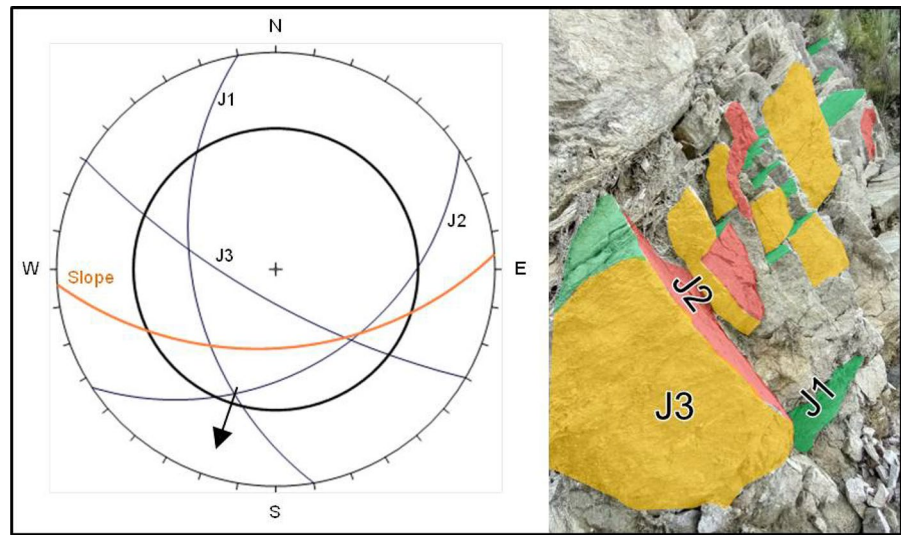


**Table 2** UCS values of the collected rock samples (modified after Tandon et al. 2022)

ID	Average diameter (D) in mm	Average width (W) in mm	Correction factor ( <i>f</i> )	Failure load (kN)	Point load strength index ( $I_s$ ) in kN/mm <sup>2</sup>	Point load strength index ( $I_{s(50)}$ ) in MPa	UCS = 24 <sup>*</sup> $I_{s(50)}$
RS1	48.73	57.4	1.08	12	0.00337	3.65	87.56
RS2	61.40	102.4	1.30	26	0.00325	4.22	101.28
RS3	50.87	50.42	1.06	14	0.00429	4.55	109.26

RQD value ( $RQD = 110 - 2.5 \times 15$ ) was estimated as 72.5. Next, the physical characteristics of joints were recorded such as close spacing ( $\sim 150$  cm), slickenside surfaces, and wet groundwater conditions. Finally, the ratings were assigned for the parameters and an  $RMR_{basic}$  value of 45 ( $(UCS = 7) + (RQD = 13) + (J. Spacing = 8) + (J. Condition = 10) + (GW = 7)$ ) representing the fair condition was given for the studied landslide. The GSI was calculated after deriving the SR and SCR values. Given the  $J_v$  of 15, the calculated SR was about ( $SR = -17.5 \ln(15) + 79.8$ ) 32 for the slope. Then, the ratings of  $R_t$  (smooth,  $R_t = 1$ ),  $R_w$  (highly weathered,  $R_w = 1$ ), and  $R_f$  (soft  $< 5$  mm,  $R_f = 2$ ) were added and the SCR is found as 4. Using the SR and SCR information, the GSI value of 25, representing the blocky disturbed rock mass was assigned for this slope. Thereafter, to derive the SMR,  $RMR_{basic}$  with  $F_1$ ,  $F_2$ ,  $F_3$ , and  $F_4$  information were integrated. From the kinematic analysis, it is observed that the probability of wedge failure is more prominent, so, the SMR was determined by considering the plunge line orientation. In this regard, the

$F_1$  ( $\alpha_i - \alpha_j = 194^\circ - 176^\circ = 18^\circ$ ),  $F_2$  ( $\beta_i = 27^\circ$ ), and  $F_3$  ( $\beta_i - \beta_s = 27^\circ - 50^\circ = -23^\circ$ ) ratings were found as 0.70, 0.40, and  $-60$ , respectively. For, the  $F_4$  factor a rating of +10 (pre-splitting condition) was considered, as the slope is already affected by past slides. Finally, the SMR value is obtained as  $SMR = 45 + (0.70 \times 0.40 \times -60) + 10 = 38.2$ , which represents the unstable slope having planar or big wedges.

Following the engineering geological investigation, geotechnical characterizations of the collected soil samples (S1 and S2) have also been carried out and the obtained results are presented in Table 3. First, the grain size analysis was performed for both the soil samples, and the percentage of soil retained in each sieve was used to find out their particle size distribution. The particle size distribution shows a greater percentage of sand ( $> 60\%$ ) with lower clay and silt ( $\sim 5\%$ ) for both samples (Table 3). The deficiency of finer particles (clay and silt) indicates that the landslide material has relatively low cohesion and high sand content in them can offer high friction angle. As per the IS 1498 : 1970 (Indian Standards)

**Table 3** Geotechnical properties of the collected soil samples

Property	S1*	S2**
Gravel (%)	17.55	31.65
Sand (%)	76.57	62.75
Clay and silt (%)	5.88	5.60
Soil classification (as per IS 1498 : 1970)	SP	SP
Maximum dry density (g/cm <sup>3</sup> )	1.62	1.77
Optimum moisture content (%)	17.44	11.36
Liquid limit (%)	30.43	34.89
Cohesion (kPa) at OMC, MDD	10	6
Friction angle (°) at OMC, MDD	30	37
Permeability (cm/s)	1.88E-04	2.39E-04

\*Soil sample was collected from the crown section

\*\*Soil sample was collected above the road section

the tested samples can be classified as poorly graded sand (SP) category. Next, the Atterberg limits were determined through the liquid limit (LL) tests. The LL was found 30.43% for S1 and 34.89% for S2 (Table 3). The LL results indicate relatively lower water content is required to reduce the shear resistance, at which soil samples will change from liquid to plastic state. Although, the plastic limit test is not performed, as the percentage of clay and silt content is fairly low for both samples (leading to non-plastic conditions). After that, the compaction test is performed and the results are shown in Table 3. Due to the dominance of sands (poorly graded) relatively lower MDD values of 1.62 g/cm<sup>3</sup> for S1 and 1.77 g/cm<sup>3</sup> for S2 were found at the OMC level of 17.44% and 11.36%, respectively. Next, from the direct shear test the obtained shear strength parameters i.e.,

cohesion (c) and friction angle (φ) for both samples are presented in Table 3.

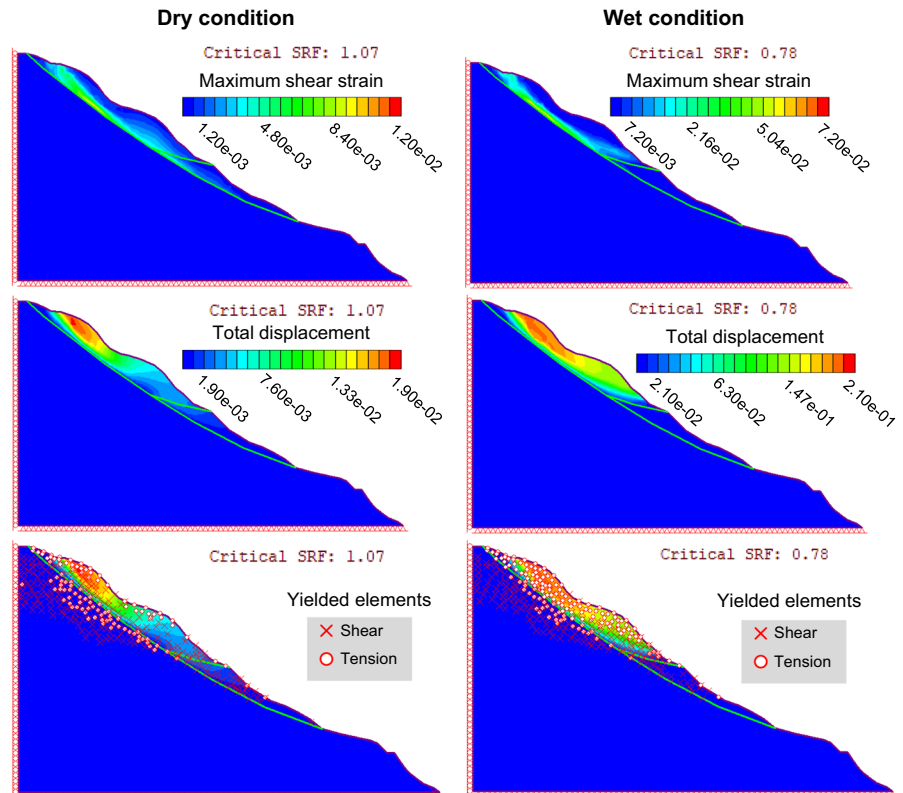
The overall assessment of the shear strength parameters reveals that the landslide material has high frictional resistance (30° for S1 and 37° for S2) with low cohesion (10 kPa for S1 and 6 kPa for S2). This is because inter-granular resistance between the soil particles (mostly in sands) increases as the applied normal stress is increased. This rate of increase conditionally depends on the cohesion between the soil particles and the saturation level. Generally, it is observed that with increasing saturation, the shear strength starts decreasing once the OMC level is achieved (Abraham et al. 2021), and thus, during rain spells high saturation leads to slope failures (Tandon et al. 2022). Along with this the rate of saturation strongly depends on the permeability characteristics and as the saturation level increases the rate of permeability starts decreasing. The results of the permeability tests show 1.88E-04 cm/sec for S1 and 2.39E-04 cm/sec for S2 and hence, can be categorized as highly permeable soil.

In the FEM module, obtained soil properties have been used as a homogeneous soil mass, and for the rock section, an equivalent continuum slope mass approach is used considering GSI derived Hoek–Brown parameters. The details of the Hoek–Brown parameters are given in Table 4. The results of the FEM analysis show critical SRF values of 1.07 for dry condition and 0.78 for wet condition ( $R_u$ ) (Fig. 9). Along with this, information on the maximum shear strain, total displacement, and distribution of yielded elements are also presented in Fig. 9. By following the obtained stability results it can be said that under the dry condition, the studied slope is marginally stable ( $1.5 \leq \text{FoS} \leq 1$ ) and as the

**Table 4** GSI based Hoek–Brown parameters (modified after Hoek and Bray 1981)

Parameters	Expressions	Remarks	Values
$m_b$	$m_b = m_i \exp\left(\frac{GSI-100}{28-14D}\right)$	$m_b$ is the Hoek–Brown material constant (rock mass), $m_i$ is the Hoek–Brown material constant (intact rock)	1.92E+00
$s$	$s = \exp\left(\frac{GSI-100}{9-3D}\right)$	$s$ and $a$ are the material constants, and their values depends on the rock mass characteristics	2.40E-04
$a$	$a = \frac{1}{2} + \frac{1}{6}(e^{-GSI/15} - e^{-20/3})$		5.31E-01
$D$ (disturbance factor)	Indicates the grade of slope excavation, blasting and/or any stress relaxation practices	Varies from 0 for undisturbed in-situ rock masses to 1 for very disturbed rock masses	0

**Fig. 9** FEM based FoS (Critical SRF) results in dry and wet ( $R_u$ ) static conditions. The figures show the maximum shear strain, total displacement, and yielded elements along the considered slope profile



saturation level increases the stability drops to unstable condition ( $FoS \leq 1$ ). Therefore, during the rainfall expectancy of failure becomes so high for this slope. Under the dry condition, maximum shear strain is concentrated at the top of the slope where loose soil debris is resting on a steep section (Fig. 9), and the intensity of shear strain increases in the wet condition, and its distribution extended in the lower part of the slope section (Fig. 9). Further, the total displacement patterns reveal the development of distinct weak zones or say slip surfaces at the top section of the slope with a maximum displacement of  $1.90e-02$  m (Fig. 9), and under the wet condition spatial extent of movement is increased and achieved a maximum displacement of  $2.10e-01$  m (Fig. 9). Next, the distribution of yielded elements is analyzed to characterize the type of failures in the considered conditions. At the dry condition, elements show tension, as well as shear failures, and these tension cracks are mostly concentrated in the top section of the slope (Fig. 9). Although some element shows both failures and thus, an overlapping symbol has appeared for them. Following their distribution, failure is observed at a

maximum depth of 30 m from the top of the slope. In contrast to the dry condition, tension failures become more prominent in the wet condition and are aligned parallel to the trailing edge of the landslide (Fig. 9). One possible reason for this can be attributed to the saturation of slope materials. Generally, saturation increases the shear strain, which leads to the formation of tension failures in the slope. The obtained result also supports the fact that the shear failure considered in the classical LEM approach may not always be suitable for all types of landslides. Although, the present study encompasses some limitations such as the soil properties were used in terms of deterministic values without considering their spatial variability. Another limitation of this study is the rock mass is modelled as an equivalent continuum. Therefore, the role of discontinuities/joints in slope stability is conservatively considered. Furthermore, to model the slope a 2D section is considered, which may affect the real world three-dimensional (3D) interpretation.

Despite these limitations, the results obtained from the applied techniques reveals that the Zero landslide has a high potentiality of failure in the near future



and the most susceptible zone is predicted below the Nimbong village area. Reactivation of landslide at this particular location can damage the upslope settlements as well as the road. Since the association of vulnerable elements increased the degree of risk, some mitigation measures can be taken for this landslide. There are two techniques generally considered while mitigating landslides: (i) increase the activity of the resisting forces (geometry modification, slope reinforcement, embankment installation, and construction of retaining walls) and (ii) reduce the driving forces (drainage measures development with geosynthetics based ground improvement). However, proper implementation of such measures requires further research in terms of suitability and effectiveness. Although, this part is not in the scope of the present study and is yet to be completed for this landslide.

## 6 Conclusions

Landslide characterization and stability assessments have the utmost importance in reducing the risk posed by them. According to Brabb (1993), at least 90% of landslide losses can be avoidable if the hazard is assessed before the event. In the present study, the Zero landslide located in the Nimbong village of Kalimpong region, Darjeeling Himalaya has been investigated. This particular landslide has gained attention due to its short temporal frequency and the associated risk elements. Therefore, a comprehensive methodology is used, explicitly intended to address the site-specific characterization and stability assessment. In order to comprehend these objectives, an extensive field investigation has been carried out, and the collected soil and rock samples are tested in the laboratory. The study also incorporates the remote sensing platform and uses earth observation satellite images to interpret the temporal behavior of this landslide. Based on these inputs empirical and numerical methods such as  $RMR_{basic}$ , GSI, SMR, and FEM analysis have been executed. Considering their results, the following conclusions are made.

- The assessment of multi-temporal satellite images shows the retrogressive progression towards the uphill slope and the recent field observation reveals that the right flank of this landslide is more active.
- The kinematic analysis indicates the development of wedge failure along the J1 and J2 by satisfying the failure conditions considered in Markland's test.
- $RMR_{basic}$  and GSI based rock mass characterization show the fair rock mass with blocky disintegrated structure. Such conditions often favour landslides when subjected to triggering factor(s).
- Following the rock mass characterization, the SMR result indicates the unstable slope, having a high potentiality of failure. Among the SMR parameters, the  $F_3$  ( $\beta_1 - \beta_3$ ) factor shows the most critical rating ( $-60$ ) and thereby indicates the underlying joint orientations have a strong influence on the stability of this slope.
- The FEM analysis suggests that the slope is marginally stable under the dry condition ( $FoS=1.07$ ); whereas, in the wet condition stability decreases by almost 26% ( $FoS=0.78$ ) and crossed the critical threshold value ( $FoS \leq 1$ ). This shows that even if the slope appears stable in dry periods, it has a chance to fail during the rainfall condition.
- The crest of the slope belonging to the soil cum debris cover shows the maximum concentration of shear strain with high displacement rates. Therefore, this area is identified as more susceptible to reactivation, which in turn increases the vulnerability of the upslope risk elements.

The present study provides a detailed overview of the Zero landslide and its stability status as well as information on the associated risks. The results suggest that the slope has a high potential for reactivation and makes a close agreement with the field observation. Such attempts may help to execute Landslide Disaster Risk Reduction (LDRR) strategies in favor of minimizing the possible damages. Along with this it is also envisaged that the adopted methodology can be applied in other landslide susceptible areas.

**Acknowledgements** The authors are grateful to the Director, CSIR-Central Building Research Institute, Roorkee for giving the permission to publish this work. The first author extends his thankfulness to the University Grants Commission, New Delhi, for providing fellowship under the Junior Research Fellowship (JRF) scheme (UGC-Ref. No. 3511/(NET-JULY 2018)) and the Academy of Scientific and Innovative Research (AcSIR), Ghaziabad for providing an opportunity to carry out his doctoral research. The first author also acknowledges the guidance received from Mr. Ajay Dwivedi (Sr. Technical Officer,

CSIR-CBRI) and Mr. Arpit Mittal (CSIR-CBRI) during the laboratory investigations of the collected samples.

**Author Contributions** Field data collection: SD; Conceptualization: SD, KP, SS, DPK; Methodology: SD, KP, SS, DPK; Numerical analysis: SD, KP; Writing - original draft preparation: SD, KP; Writing - review and editing: SS, DPK; Resources: SS, DPK; Supervision: SS, DPK.

**Funding** This research did not receive any specific Grant from funding agencies in the public, commercial, and/or not-for-profit sectors.

**Data Availability** The datasets generated during and/or analysed in this study are available from the corresponding author on reasonable request.

**Code Availability** Not applicable.

## Declarations

**Conflict of interest** The authors declare that they have no known conflicts of interests or personal relationships that could have appeared to influence the work reported in this paper.

## References

- Abraham MT, Satyam N, Reddy SKP, Pradhan B (2021) Runout modeling and calibration of friction parameters of Kurichermala debris flow, India. *Landslides* 18(2):737–754. <https://doi.org/10.1007/s10346-020-01540-1>
- Anbalagan R, Sharma S, Raghuvanshi TK (1992) Rock mass stability evaluation using modified SMR approach. In: 6th national symposium on rock mechanics. Proceedings, Bangalore, India, pp 258–268
- Ansari TA, Sharma KM, Singh TN (2019) Empirical slope stability assessment along the road corridor NH-7, in the lesser Himalayan. *Geotech Geol Eng* 37:5391–5407. <https://doi.org/10.1007/s10706-019-00988-w>
- Bhattacharyya K, Mitra G, Kwon S (2015) Geometry and kinematics of the Darjeeling–Sikkim Himalaya, India: implications for the evolution of the himalayan fold-thrust belt. *J Asian Earth Sci* 113:778–796. <https://doi.org/10.1016/j.jseae.2015.09.008>
- Bieniawski ZT (1989) *Engineering rock mass classifications: a complete manual for engineers and geologists in mining, civil, and petroleum engineering*. Wiley, New Jersey
- Bishop AW, Morgenstern N (1960) Stability coefficients for earth slopes. *Geotechnique* 10(4):129–153
- Brabb EE (1993) Proposal for worldwide landslide hazard maps. In: proceedings of 7th international conference and field workshop on landslide in Czech and Slovak Republics, pp 15–27
- Cruden DM, Varnes DJ (1996) *Landslides: investigation and mitigation*. Chapter 3-Landslides types and processes, vol 247. Transportation research board special report, pp 36–75
- Das S, Sarkar S, Kanungo DP (2022) GIS-based landslide susceptibility zonation mapping using the analytic hierarchy process (AHP) method in parts of Kalimpong Region of Darjeeling Himalaya. *Environ Monit Assess* 194(3):1–28. <https://doi.org/10.1007/s10661-022-09851-7>
- Dash RK, Kanungo DP, Malet JP (2021) Runout modelling and hazard assessment of Tangni debris flow in Garhwal Himalayas, India. *Environ Earth Sci* 80(9):1–19. <https://doi.org/10.1007/s12665-021-09637-z>
- Fukushima Y, Tanaka T (1990) A new attenuation relation for peak horizontal acceleration of strong earthquake ground motion in Japan. *B Seismol Soc Am* 80(4):757–783
- Hoek E, Bray JW (1981) *Rock Slope Engineering, Revised, 3rd edn*. The Institution of Mining and Metallurgy, London, pp 341–351
- Hu CM, Yuan YL, Mei Y, Wang XY, Liu Z (2019) Modification of the gravity increase method in slope stability analysis. *B Eng Geol Environ* 78(6):4241–4252. <https://doi.org/10.1007/s10064-018-1395-2>
- IS 1498 : 1970 (Reviewed In : 2021) Classification and identification of soils for general engineering purposes [CED, vol 43. Soil and Foundation Engineering]
- IS 1893 (Part 1) : 2016 (Reviewed In : 2021) Criteria for earthquake resistant design of structures - Part 1: general provisions and buildings [CED, vol 39. Earthquake Engineering]
- Kanungo DP, Arora MK, Gupta RP, Sarkar S (2008) Landslide risk assessment using concepts of danger pixels and fuzzy set theory in Darjeeling Himalayas. *Landslides* 5:407–416. <https://doi.org/10.1007/s10346-008-0134-3>
- Kanungo DP, Pain A, Sharma S (2013) Finite element modeling approach to assess the stability of debris and rock slopes: a case study from the Indian Himalayas. *Nat Hazards* 69(1):1–24. <https://doi.org/10.1007/s11069-013-0680-4>
- Kumar V, Gupta V, Jamir I, Chatteraj SL (2019) Evaluation of potential landslide damming: case study of Urni landslide, Kinnaur, Satluj valley, India. *Geosci Front* 10(2):753–767. <https://doi.org/10.1016/j.gsf.2018.05.004>
- Malamud BD, Turcotte DL, Guzzetti F, Reichenbach P (2004) Landslide inventories and their statistical properties. *Earth Surf Proc Land* 29(6):687–711. <https://doi.org/10.1002/esp.1064>
- Mandal P, Sarkar S (2021) Estimation of rainfall threshold for the early warning of shallow landslides along National Highway-10 in Darjeeling Himalayas. *Nat Hazards* 105(3):2455–2480. <https://doi.org/10.1007/s11069-020-04407-9>
- Martha TR, Roy P, Jain N, Vinod Kumar K, Reddy PS, Nalini J et al (2021) Rock avalanche induced flash flood on 07 February 2021 in Uttarakhand, India—A photogeological reconstruction of the event. *Landslides* 18(8):2881–2893. <https://doi.org/10.1007/s10346-021-01691-9>
- Matsui T, San KC (1992) Finite element slope stability analysis by shear strength reduction technique. *Soils Found* 32(1):59–70
- Pain A, Kanungo DP, Sarkar S (2014) Rock slope stability assessment using finite element based modelling—examples from the Indian Himalayas. *Geomech Geoeng* 9(3):215–230. <https://doi.org/10.1080/17486025.2014.883465>
- Palmstrom A (2005) Measurements of and correlations between block size and rock quality designation (RQD).

- Tunn Undergr Sp Tech 20(4):362–377. <https://doi.org/10.1016/j.tust.2005.01.005>
- Panda SD, Kumar S, Pradhan SP, Singh J, Kralia A, Thakur M (2022) Effect of groundwater table fluctuation on slope instability: a comprehensive 3D simulation approach for Kotropi landslide, India. *Landslides*. <https://doi.org/10.1007/s10346-022-01993-6>
- Romana M (1985) New adjustment ratings for application of Bieniawski classification to slopes. In: proceedings of the international symposium on role of rock mechanics, Zacatecas, Mexico, pp 49–53
- Sardana S, Sinha RK, Verma AK, Jaswal M, Singh TN (2022) A semi-empirical approach for rockfall prediction along the Lengpui-Aizawl Highway Mizoram, India. *Geotech Geol Eng* 40(11):5507–5525. <https://doi.org/10.1007/s10706-022-02229-z>
- Sarkar S, Pandit K, Dahiya N, Chandna P (2021) Quantified landslide hazard assessment based on finite element slope stability analysis for Uttarkashi–Gangnani Highway in Indian Himalayas. *Nat Hazards* 106(3):1895–1914. <https://doi.org/10.1007/s11069-021-04518-x>
- Scheidegger AE (1973) On the prediction of the reach and velocity of catastrophic landslides. *Rock Mech* 5(4):231–236. <https://doi.org/10.1007/BF01301796>
- Singh AK, Kundu J, Sarkar K (2018) Stability analysis of a recurring soil slope failure along NH-5, Himachal Himalaya, India. *Nat Hazards* 90(2):863–885. <https://doi.org/10.1007/s11069-017-3076-z>
- Song ZC, Zhao LH, Li L, Zhang Y, Tang G (2018) Distinct element modelling of a landslide triggered by the 5.12 Wenchuan earthquake: a case study. *Geotech Geol Eng* 36:2533–2551. <https://doi.org/10.1007/s10706-018-0481-3>
- Sonmez H, Ulusay R (2002) A discussion on the Hoek-Brown failure criterion and suggested modifications to the criterion verified by slope stability case studies. *Yerbilimleri* 26(1):77–99
- Tandon RS, Gupta V, Venkateshwarlu B, Joshi P (2022) An assessment of Dungale landslide using remotely piloted aircraft system (RPAS), ground penetration radar (GPR), and Slide & RS2 Softwares. *Nat Hazards*. <https://doi.org/10.1007/s11069-022-05334-7>
- Tesfa C (2022) GIS-Based AHP and FR methods for Landslide susceptibility mapping in the Abay Gorge, Dejen–Renaissance Bridge, Central, Ethiopia. *Geotech Geol Eng* 40(10):5029–5043. <https://doi.org/10.1007/s10706-022-02197-4>
- Walsh RPD, Lawler DM (1981) Rainfall seasonality: description, spatial patterns and change through time. *Weather* 36(7):201–208. <https://doi.org/10.1002/j.1477-8696.1981.tb05400.x>

**Publisher's Note** Springer Nature remains neutral with regard to jurisdictional claims in published maps and institutional affiliations.

Springer Nature or its licensor (e.g. a society or other partner) holds exclusive rights to this article under a publishing agreement with the author(s) or other rightsholder(s); author self-archiving of the accepted manuscript version of this article is solely governed by the terms of such publishing agreement and applicable law.